DIRECT NUMERICAL SIMULATION OF GAS–SOLIDS FLOW BASED ON THE IMMERSED BOUNDARY METHOD

Authors: Rahul Garg[1], Sudheer Tenneti[1], Jamaludin Mohd.-Yusof[2], Shankar Subramaniam[1]

[1] Department of Mechanical Engineering, Iowa State University, U.S.A.
[2] CCS-2, Computational Physics & Methods
Computer, Computational & Statistical Sciences
Los Alamos National Laboratory, U.S.A

MOMENTUM TRANSFER IN GAS-SOLIDS FLOW

Accurate representation of the momentum transfer between particles and fluid is necessary for predictive simulation of gas-solids flow in industrial applications. Such device-level simulations are typically based on averaged equations of mass and momentum conservation corresponding to the fluid and particle phase(s) in gas-solids flow (Syamlal, Rogers, & O'Brien, 1993), and these constitute the multi-fluid theory. The momentum conservation equation in this theory contains a term representing the average interphase momentum transfer between particles and fluid. The dependence of this term on flow quantities such as the Reynolds number based on mean slip velocity, solid volume fraction, and particle size distribution must be modeled in order to solve the set of averaged equations, and is simply referred to as a drag law. If higher levels of statistical representation are adopted—such as the second moment of particle velocity, or the particle distribution function—then the corresponding terms (such as the interphase transfer of kinetic energy in the second velocity moment equations) appearing in those equations also need to be modeled.

Direct numerical simulation of flow past particles is a first-principles approach to developing accurate models for interphase momentum transfer in gas-solids flow at all levels of statistical closure. Since DNS solves the governing Navier-Stokes equations with exact boundary conditions imposed at each particle surface, it produces a model free solution with complete three dimensional time-dependent velocity and pressure fields. In principle, all Eulerian and Lagrangian flow statistics can be extracted from the DNS data making it a powerful tool for model validation and development (Pope, 2000; Rai, Gatski, & Erlebacher, 1995). While there are different numerical approaches available to perform DNS of gas-solids flow—such as the lattice Boltzmann method (LBM)—here we describe a DNS approach that is based on the immersed boundary method (IBM). The outline of this chapter is as follows. We first describe the context in which models for interphase momentum transfer arise. We begin with the transport equation for the one-particle distribution function that is the starting point for the kinetic theory of granular and multiphase flows. This is appropriate because all moment-based theories (averaged

equations, second and higher moments) can be derived from this distribution function. Thus, by developing closure models at the level of the one-particle distribution function, we effectively model all moment equations. The appropriate physical problem that needs to be set up to approximate statistically homogeneous gas-solid suspension flow is then described. The expression for the mean interphase momentum transfer term in steady, homogeneous, gas-solids flow that arises from the averaged conservation equations in the two-fluid theory is then derived, and related to the equivalent term in the one-particle distribution function approach. Then the immersed boundary method and its implementation are described. Numerical error associated with forming statistical estimates of the interphase momentum transfer term is analyzed and decomposed into spatial, temporal and statistical contributions. This results in the identification of relevant numerical parameters (grid resolution, size of computational domain, number of particle configurations) corresponding to each of the error contributions. Numerical convergence of the IBM DNS code is established, and results from standard tests are presented that validate the simulation approach. Drag laws obtained from IBM simulations are discussed and compared with those obtained from other simulation methods. The IBM approach is compared with other simulation approaches, and relative advantages and disadvantages are discussed. Directions for further research in the formulation of models of gas-solids flow using DNS based on IBM are outlined. Finally, the contributions of this chapter are summarized along with concluding remarks regarding the use of IBM for direct numerical simulation of gas-solids flow.

Transport of the particle distribution function

The transport equation for the one-particle distribution function in gas-solids flow for monodisperse particles is (Chapman & Cowling, 1952; Garzo, Hrenya, & Dufty, 2007; Jenkins, 1998; Koch, 1990; Liboff, 1990; Subramaniam, 2001)

$$\frac{\partial f}{\partial t}+\frac{\partial}{\partial x_k}(v_k f)+\frac{\partial}{\partial v_k}(\langle A_k \,|\, \mathbf{x},\mathbf{v},t\rangle f)=\dot{f}_{coll} \tag{1.1}$$

where $\mathbf{v}$ is the velocity of the particles, $\langle \mathbf{A} \,|\, \mathbf{x},\mathbf{v},t\rangle$ is the conditional expectation of the acceleration and $\dot{f}_{coll}$ is the term arising due to collisions between particles.

The principal difference between this equation for solid particles and its counterpart in molecular gases is the appearance of the conditional expectation of the acceleration $\langle \mathbf{A} \,|\, \mathbf{x},\mathbf{v},t\rangle$ inside the velocity derivative corresponding to transport of the distribution function in velocity space. The conditional expectation of acceleration cannot be expressed purely in terms of the distribution function, and is hence denoted an unclosed term in the above equation. It can depend on higher-order distribution functions (e.g., the two-particle distribution function) in the hierarchy resulting from a description of the particle system in terms of the Liouville density. It also depends on statistics of the carrier flow. Since analytical models are difficult to propose for this term beyond dilute particle flow in the Stokes flow regime, it must be inferred from direct numerical simulation data. Drag laws for steady flow through homogeneous suspensions are obtained by integrating the conditional expectation of the acceleration over velocity space to obtain the average force $\langle \mathbf{F}_d \rangle$ exerted on the particles by the fluid

$$\langle F_{d,i} \rangle = \frac{m}{n}\int \langle A_i \,|\, \mathbf{v}\rangle f d\mathbf{v}\,, \tag{1.2}$$

where m is the mass of a particle, and n is the particle number density.

Homogeneous suspension flow

In order to calculate $\langle \mathbf{F}_d \rangle$ from DNS, it is natural to simulate a statistically homogeneous suspension flow with freely moving particles, and to then compute volume-averaged estimates of $\langle \mathbf{F}_d \rangle$ from particle acceleration data. Imposing a mean pressure gradient to balance the weight of the particles leads to a steady mean momentum balance. In this setup the particle positions and velocities sample a trajectory in phase space that corresponds to the specified nonequilibrium steady state, and time averaging can be used to improve the estimate for $\langle \mathbf{F}_d \rangle$. However, such freely moving suspensions are computationally prohibitive especially because in order to propose drag laws these simulations need to be performed over a range of solid volume fractions and mean flow Reynolds numbers (based on mean slip velocity). Furthermore, over a wide range of volume fraction and particle Stokes number, the particle configuration in individual realizations develops spatial structures due to flow instabilities. Wylie and Koch (Wylie & Koch, 2000) performed simulations of a suspension with particles moving along ballistic trajectories between elastic hard sphere collisions, but this assumption that the fluid does not affect the particle motion is valid only in the limit of high Stokes number.

Koch and Hill (Koch & Hill, 2001) discuss the relevant non-dimensional parameters that arise in the context of gas-solid suspensions. As noted in their work, direct numerical simulations are useful in developing drag laws for suspension flows where the effects of fluid inertia and the particle inertia cannot be neglected. In the simulations described in this work we neglect gravity, so the relevant nondimensional parameters are the Reynolds number (characterizing the importance of fluid inertia) and the particle Stokes number (characterizing the importance of particle inertia). While the Stokes flow regime (negligible fluid inertia) is amenable to analytical treatment, direct simulation is the only approach for gas-solid suspensions at finite Reynolds number.

Steady flow past homogeneous assemblies of fixed particles

A convenient simplification for high Stokes number suspensions is to replace the ensemble of particle positions and velocities sampled by the system in its nonequilibrium steady state, by a set of particle configurations and velocities that would result from a granular gas simulation. Steady flow past fixed assemblies of particles in configurations (and with velocities) sampled from this set is simulated, and drag laws are obtained by averaging over this ensemble. The idea of extracting drag laws from steady flow past random and ordered arrays of particles through particle assemblies has been successfully exploited by several researchers using the LBM simulation methodology developed by Ladd (Ladd, 1994a, 1994b) for particulate suspensions. For example, Koch and co-workers (Hill, Koch, & Ladd, 2001a) and (Hill, Koch, & Ladd, 2001b), referred to collectively as HKL, studied the steady flow past both ordered and random arrays. Kuipers and co-workers (van der Hoef, Beetstra, & Kuipers, 2005) and (Beetstra, van der Hoef, & Kuipers, 2007), collectively referred to as BVK, extended HKL's LBM simulations to higher Reynolds numbers.

In the simplest case of a monodisperse suspension, the drag law is extracted by computing steady nonturbulent flow at a specified mean slip Reynolds number past a set of random particle configurations (microstates) that correspond to a particular value of the solid volume fraction. The pair-correlation and higher-order statistics of the particle field are determined by the configurations resulting from the granular gas simulation. The particle velocity distribution can be initialized either from the granular gas simulation at finite granular temperature or it is often assumed that all particles move with the same velocity.

GOVERNING EQUATIONS

The schematic in corresponds to the physical problem of flow past a single particle. Volumes occupied by the fluid and solid phases are denoted by $\mathcal{V}_\mathrm{f}$ and $\mathcal{V}_\mathrm{s}$ respectively, such that the total domain volume $\mathcal{V} = \mathcal{V}_\mathrm{f} + \mathcal{V}_\mathrm{s}$. The bounding surface of the physical domain is denoted $\partial\mathcal{V}$, and the bounding surfaces of the solid phase and fluid phase are denoted by $\partial\mathcal{V}_\mathrm{s}$ and $\partial\mathcal{V}_\mathrm{f}$, respectively. For incompressible flows, the mass and momentum conservation equations for the fluid-phase are

$$\frac{\partial u_i}{\partial x_i} = 0 \tag{1.3}$$

and

$$\rho_\mathrm{f}\frac{\partial u_i}{\partial t} + \rho_\mathrm{f}\frac{\partial u_i u_j}{\partial x_j} = -g_i + \mu_\mathrm{f}\frac{\partial^2 u_i}{\partial x_j \partial x_j} = \frac{\partial \tau_{ji}}{\partial x_j} \tag{1.4}$$

respectively. In the above equation $\mathbf{g} = \nabla p$ is the gradient of modified pressure (Mohd-Yusof, 1996), and ρ_f and μ_f are the thermodynamic density and dynamic viscosity of the fluid-phase, respectively. At the particle-fluid interface, in order to ensure zero slip and zero penetration (for impermeable surfaces) boundary conditions, the relative velocity should be zero. If the solid particles are held stationary, then the above boundary conditions translate to

$$\mathbf{u} = 0 \text{ on } \partial\mathcal{V}_\mathrm{s}. \tag{1.5}$$

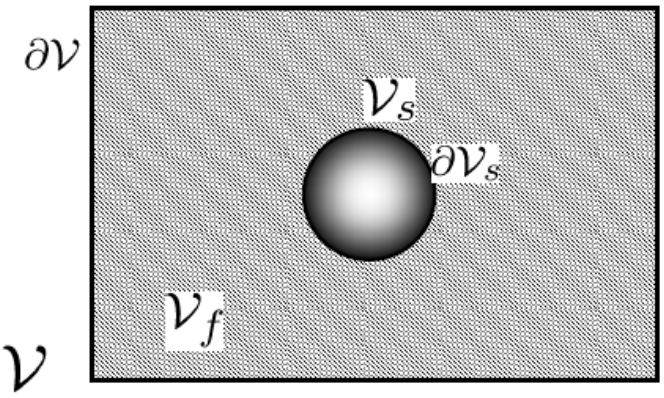

Figure 1: Schematic of the physical domain with only one particle. Hatched lines represent the volume $\mathcal{V}_\mathrm{f}$ occupied by the fluid-phase and solid fill represents the volume $\mathcal{V}_\mathrm{s}$ of the solid-phase

such that the total volume of physical domain $\mathcal{V} = \mathcal{V}_\mathrm{f} + \mathcal{V}_\mathrm{s}$. *The bounding surfaces of the physical domain, solid-phase, and fluid-phase are denoted by* $\partial\mathcal{V}$, $\partial\mathcal{V}_\mathrm{s}$, *and* $\partial\mathcal{V}_\mathrm{f}$, *respectively.*

The averaged equations corresponding to these mass and momentum conservation balances are useful in simulations of practical gas-solids flow applications. In the previous section we described one statistical approach based on the one-particle distribution function. Here we first describe an alternative approach called the Eulerian two-fluid theory because it is more natural to derive the averaged equations corresponding to Eq. (1.4) using this approach. The conditional expectation of acceleration appearing in the one-particle distribution function approach is then related to the mean interphase momentum transfer term in the Eulerian two-fluid theory.

In the Eulerian two-fluid theory phasic averages are defined as follows. If $Q(\mathbf{x},t)$ is any field, then its phasic average $\left\langle Q^{(f)} \right\rangle(\mathbf{x},t)$ over the fluid volume $\mathcal{V}_\mathrm{f}$, referred to as fluid-phase mean, is defined as:

$$\left\langle Q^{(f)} \right\rangle(\mathbf{x},t) = \frac{\left\langle I_f(\mathbf{x},t) Q(\mathbf{x},t) \right\rangle}{\left\langle I_f(\mathbf{x},t) \right\rangle}, \tag{1.6}$$

where I_f is the fluid-phase indicator function which is equal to one if the point $\mathbf{x}$ lies in the fluid phase, and zero otherwise.

The solid-phase mean $\left\langle Q^{(s)} \right\rangle(\mathbf{x},t)$ is similarly defined. The (unconditional) mixture mean $\left\langle Q \right\rangle(\mathbf{x},t)$ is related to the phasic mean by:

$$\left\langle Q \right\rangle = \varepsilon_\mathrm{f} \left\langle Q_\mathrm{f} \right\rangle + \varepsilon_\mathrm{s} \left\langle Q_\mathrm{s} \right\rangle \tag{1.7}$$

where $\varepsilon_\mathrm{f} = \left\langle I_f(\mathbf{x},t) \right\rangle$ and $\varepsilon_\mathrm{s} = \left\langle I_s(\mathbf{x},t) \right\rangle$ are the volume fractions of the fluid and solid phases, respectively. If the flow is statistically homogeneous, there is no dependence on $\mathbf{x}$ and spatial derivatives are zero. Similarly, if the flow is statistically stationary there is no dependence on t and temporal derivatives are zero.

The mean momentum conservation equation (Drew & Passman, 1999; Pai & Subramaniam, 2009) in the fluid phase is obtained by multiplying the momentum conservation equation (1.4) by I_f resulting in

$$\frac{\partial \rho_\mathrm{f} \varepsilon_\mathrm{f} \left\langle u_i^{(f)} \right\rangle}{\partial t} + \frac{\partial}{\partial x_j} \rho_\mathrm{f} \varepsilon_\mathrm{f} \left\langle u_i^{(f)} \right\rangle \left\langle u_j^{(f)} \right\rangle = \frac{\partial}{\partial x_j} \left\langle I_f u''^{(f)}_i u''^{(f)}_j \right\rangle + \left\langle I_f \frac{\partial \tau_{ji}}{\partial x_j} \right\rangle, \tag{1.8}$$

where $u''^{(f)}_i = u_i - \left\langle u_i^{(f)} \right\rangle$ is the fluctuating component of the fluid velocity field. For steady flow with an imposed mean pressure gradient in the fluid phase, it is convenient to decompose the pressure gradient term that appears in the divergence of the fluid-phase stress tensor as $\mathbf{g} = \left\langle \mathbf{g} \right\rangle + \mathbf{g}'$, such that remaining part of the stress tensor τ'_{ji} is defined by the expression:

$$\frac{\partial \tau_{ji}}{\partial x_j} = -\left\langle g_i \right\rangle - g'_i \; + \mu_\mathrm{f} \frac{\partial^2 u_i}{\partial x_j \partial x_j} = -\left\langle g_i \right\rangle + \frac{\partial \tau'_{ji}}{\partial x_j}. \tag{1.9}$$

For a statistically homogeneous suspension at steady state (statistically stationary flow), the average velocity does not depend on $\mathbf{x}$ or t, and the unsteady and convective terms on the left hand side of Eq. (1.8) do not contribute. Writing the remaining terms in an integral form, shows that the mean pressure gradient term $\varepsilon_f \langle \mathbf{g} \rangle$ balances the sum of fluctuating pressure and viscous stress on the solid particles:

$$\varepsilon_{\mathrm{f}} \langle g_i \rangle = -\left\langle \tau'_{ji} n_j^{(s)} \delta(\mathbf{x} - \mathbf{x}^{(I)}) \right\rangle . \tag{1.10}$$

In the above equation $n_j^{(s)}$ is the normal vector pointing outward from the particle surface into the fluid, and the stress tensor is evaluated on the fluid side of the interface. The term $-\left\langle \tau'_{ji} n_j^{(s)} \delta(\mathbf{x} - \mathbf{x}^{(I)}) \right\rangle$ appears as the drag contribution $F_{gm}(\mathbf{v}_{sm} - \mathbf{v}_g)$ to the fluid-solids interaction force $\mathbf{I}_{gm}$ in the two-fluid equations derived from a volume-averaging approach (Syamlal et al., 1993). For statistically homogeneous flows, the relationships between the one-particle distribution function approach and the Eulerian two-fluid theory are established in the context of a comprehensive probability density function approach to multiphase flows (Pai & Subramaniam, 2009). Using the relationships in Pai & Subramaniam (2009), it is easy to show that the term on the right hand side of Eq. (1.10) is related to the average force exerted by the fluid on the particles (see Eq. (1.2)) as follows:

$$\left\langle F_{d,i} \right\rangle = m \left\langle A_i \right\rangle = \frac{1}{n} \left\{ -\varepsilon_{\mathrm{s}} \langle g_i \rangle + \left\langle \tau'_{ji} n_j^{(s)} \delta(\mathbf{x} - \mathbf{x}^{(I)}) \right\rangle \right\}. \tag{1.11}$$

THE IMMERSED BOUNDARY METHOD

The basic notion of the immersed boundary method is to apply a set of forces on the computational grid to mimic the presence of an interface. This has several advantages over conventional boundary or body-fitted grids, especially for problems involving moving interfaces. First, there is no overhead for grid generation, which can add considerable computational expense even for non-deforming geometries. Second, the convergence of the solvers is generally better for Cartesian meshes than for unstructured meshes. Third, IBM is intended to be implemented on regular Cartesian meshes that require much less storage overhead than general unstructured or curvilinear meshes. The primary disadvantage of IBM is the reduced resolution near the interface, but this is remedied by adopting adaptive mesh techniques. There are two basic facets of the IBM, namely the choice of flow field (i.e. what velocity field do we wish to achieve) and calculation of the force itself (i.e. once we decide on the field we wish to achieve, how do we specify the force at each time-step). For clarity we will separate these two aspects, dealing with the force specification first.

The immersed boundary method was originally developed by Peskin (Peskin, 1982) as a way to incorporate the effect of flexible interfaces into fluid simulations. In that version, the local force is obtained from some constitutive relation commensurate with the nature of the interface (e.g surface tension in the case of a bubble, Young's modulus for an elastic membrane) and is, by necessity, iterative over a timestep since the location of the interface is not known *a priori*. This method has been applied to a variety of flows, such as bubbles, blood cells and swimming fish. The issue with this implementation is that it is not efficient for rigid bodies, since this requires driving the stiffness of the interface membrane (and effectively the stiffness of the equations to be

solved) to infinity. The same is true for the Immersed Interface method (IIM) which is well suited to the solution to the flow past deformable bodies (Lee & Leveque, 2003). .

Goldstein (Goldstein, Handler, & Sirovich, 1993) proposed what is essentially proportional-integral feedback on the force term to produce boundary conditions on a rigid body. The problem with this method is the lack of efficiency; due to the need to numerically integrate the force in (pseudo-continuous) time over a single time-step, the effective CFL limit was extremely small, ($O(10^{-3})$). Coincident with Goldstein's work, Mohd-Yusof (Yusof, 1996) developed what is now termed the Discrete-Time Immersed Boundary Method (DTIBM). The essential aspect of this formulation is the recognition that examination of the discretized-in-time equations leads to a straightforward definition of the force at a given point, once we have decided on the required velocity field (and hence the velocity required at the point in question).

We now turn our attention to the choice of flow field. The implementations to date can be broadly divided into two classes; ghost fluid and numerical boundary layers. In the former, the flow field in the region of interest is extrapolated across the interface in such a way as to impose the desired boundary condition at the interface. This is the method used in the original implementations of Goldstein and Mohd-Yusof, as well as in this chapter. Such an implementation is natural in situations where the fictitious flow produced within the rigid body does not affect the solution and is easily accounted for. This choice has the advantage that the force applied in the fluid region can be zero; that is, the governing equations are unmodified in this region. Additionally, the use of the ghost fluid region allows the effect of, for example, implicit diffusion operators, to be minimized by forcing linear velocity gradients across the interface.

In the latter method, the immersed boundary force applied at the interface is numerically smoothed over several grid-points, for numerical stability reasons. As used by Peskin, this is a natural implementation, since the flow on both sides of the interface is required for the solution. It is possible to use the numerical boundary layer formulation for rigid body problems, as was done by Verzicco et. al. (Verzicco, Mohd-Yusof, Orlandi, & Haworth, 2000) where the discrete-time formulation of Mohd-Yusof was applied with numerical boundary layers in the fluid side, and with exact rigid body fields imposed in the solid.

Solution Approach

In the immersed boundary method, the mass and momentum equations are solved in the entire domain that includes the interior regions of the solid particles as well. The mass and momentum conservation equations solved in IBM are

$$\frac{\partial u_i}{\partial x_i} = 0 \tag{1.12}$$

and

$$\frac{\partial u_i}{\partial t} + S_i = -\frac{1}{\rho_{\mathrm{f}}} g_{\mathrm{IBM},i} + \nu_{\mathrm{f}} \frac{\partial^2}{\partial x_j \partial x_j} u_i + f_{\mathrm{u},i} \tag{1.13}$$

respectively, $\nu_{\mathrm{f}} = \dfrac{\mu_{\mathrm{f}}}{\rho_{\mathrm{f}}}$ is the kinematic viscosity, $\mathbf{g}_{\mathrm{IBM}}$ is the pressure gradient, $\mathbf{S} = \nabla\cdot(\mathbf{uu})$ is the convective term in conservative form, and $\mathbf{u}$ is the instantaneous velocity field. In the above momentum conservation equation, $\mathbf{f}_{\mathrm{u}}$ is the additional immersed boundary force term that accounts for the presence of solid particles in the fluid-phase by ensuring zero slip and zero penetration boundary conditions (Eq. (1.5)) at the particle-fluid interface.

In Figure 2, a schematic describing the computation of the immersed boundary forcing is shown. The surface of the solid particle is represented by a discrete number of points called boundary points, by discretizing the sphere in spherical coordinates. Another set of points called exterior points are generated by projecting these boundary points onto a sphere of radius $r + \Delta r$, where r is the radius of the particle. Similarly, the boundary points are projected onto a smaller sphere of radius $r - \Delta r$ and these points are called interior points. In our simulations, Δr is taken to be same as the grid spacing. The immersed boundary force is computed only at the interior points. At these points, the fluid velocity field is forced in a manner similar to the ghost cell approach used in standard finite-difference/finite-volume based methods. Or more specifically for the case of zero solid particle velocity, the velocity field inside the solid particle at grid points close to the interface is forced to be exact opposite of the fluid velocity field outside the particle (see Figure 2). The details of this forcing approach are discussed in Yusof (Yusof, 1996). In Yusof's original implementation, the IB forcing was also computed on the boundary points in addition to the interior points. The IB forcing at the boundary points was then interpolated to the neighboring grid nodes that could include grid nodes in the fluid phase. This additional forcing leads to contamination of the fluid velocity and pressure fields by the IB forcing. In the current implementation of DTIBM, we are able to obtain accurate results even with zero forcing at the boundary points, avoiding any contamination of the fluid velocity and pressure fields by IB forcing. It is noteworthy that the discretization of the sphere in spherical coordinates is independent of the grid resolution and hence to some extent, decouples the grid resolution from the accuracy with which the boundary condition is imposed. In addition to forcing the velocity field, the IB forcing term also cancels the remaining terms in the momentum conservation and, at the $n+1$ time-step, it is given by

$$f_{\mathrm{u},i}^{n+1} = \frac{u_i^d - u_i^n}{\Delta t} - S_i^n + g_i^n - \nu_{\mathrm{f}} \frac{\partial^2}{\partial x_j \partial x_j} u_i^n \tag{1.14}$$

where u_i^d is the desired velocity at that location.

Since the immersed boundary force $\mathbf{f}_{\mathrm{u}}$ is a function of both space and time, its effect on the pressure field is accounted by solving a modified pressure Poisson equation given by

$$\frac{1}{\rho_{\mathrm{f}}} \frac{\partial g_{\mathrm{IBM},i}}{\partial x_i} = -\frac{\partial}{\partial x_i}(S_i - f_{\mathrm{u},i}), \tag{1.15}$$

which is obtained by taking the divergence of the instantaneous momentum conservation equation (1.13) and using the mass conservation equation (1.12).

For flow past a statistically homogeneous particle assembly, we solve the IBM governing equations by imposing periodic boundary conditions on fluctuating variables that are now

defined. From the definition of volumetric mean, the velocity field $\mathbf{u}(\mathbf{x},t)$ can be decomposed as the sum of a volumetric mean $\langle \mathbf{u} \rangle_{\mathcal{V}}$ and a fluctuating component $\mathbf{u}'(\mathbf{x},t)$

$$u_i(\mathbf{x},t) = \langle u_i \rangle_{\mathcal{V}}(t) + u_i'(\mathbf{x},t), \tag{1.16}$$

and similar decompositions are written for the non-linear term $\mathbf{S}$, pressure gradient $\mathbf{g}_{\mathrm{IBM}}$, and immersed boundary forcing $\mathbf{f}_{\mathrm{u}}$ terms. Substituting the above decompositions in the mass (1.12) and momentum (1.13) conservation equations, followed by volume averaging, yields the volume-averaged mass and momentum conservation equations. Since the volumetric means are independent of $\mathbf{x}$, mean mass conservation is trivially satisfied. The volume-averaged momentum conservation equation becomes

$$\frac{\partial \langle u_i \rangle_{\mathcal{V}}}{\partial t} = -\frac{1}{\rho_{\mathrm{f}}} \langle g_{\mathrm{IBM},i} \rangle_{\mathcal{V}} + \langle f_{\mathrm{u},i} \rangle_{\mathcal{V}}, \tag{1.17}$$

where it is noted that due to periodic boundary conditions, the volume integrals of convective and diffusive terms are zero.

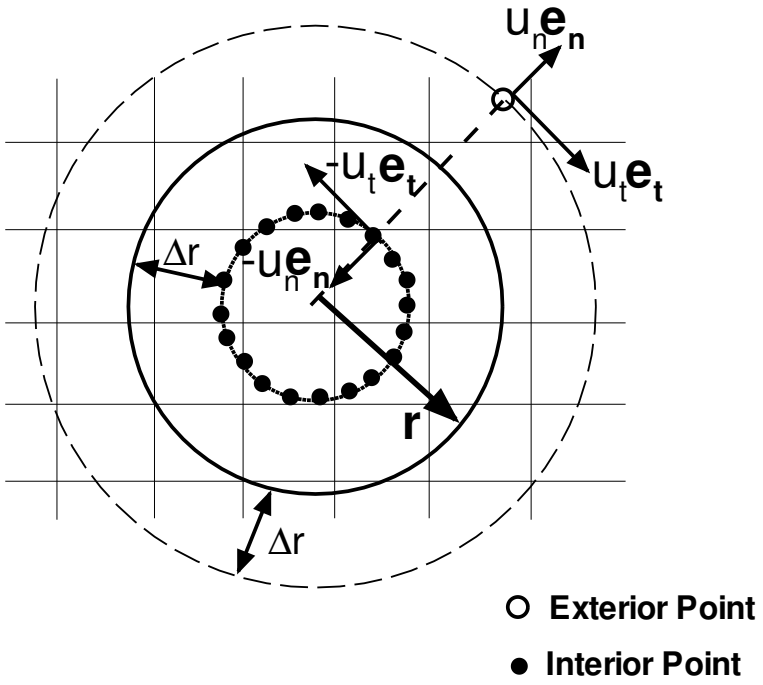

Figure 2: A schematic showing the computation of the immersed boundary forcing for a stationary particle. The solid circle represents the surface of the particle at r. Open dot shows the location of one exterior point at r+Δr (only one exterior point is shown for clarity, although there is one exterior point for each interior point) and filled dots show the location of interior points at r-Δr where the immersed boundary forcing is computed. For the special case of a stationary particle, the velocity at the interior points is forced to be the opposite of the velocity at the corresponding exterior points.

While mean mass conservation (in the volume-averaged sense) is trivially satisfied, the fluctuating velocity field needs to be divergence free

$$\frac{\partial u_i'}{\partial x_i} = 0 \,. \tag{1.18}$$

Subtracting the volume-averaged momentum conservation equation from the instantaneous momentum conservation equation (1.13) yields the following equation for the conservation of fluctuating momentum:

$$\frac{\partial u_i'}{\partial t} + S_i' = -\frac{1}{\rho_{\mathrm{f}}} g_i' + \nu_{\mathrm{f}} \frac{\partial^2}{\partial x_j \partial x_j} u_i' + f_{\mathrm{u},i}' \,. \tag{1.19}$$

Taking the divergence of the above equation and using (1.18) results in the following modified pressure Poisson equation for the fluctuating pressure gradient:

$$\frac{1}{\rho_{\mathrm{f}}} \frac{\partial g_{\mathrm{IBM},i}'}{\partial x_i} = -\frac{\partial}{\partial x_i} (S_i' - f_{\mathrm{u},i}') \,. \tag{1.20}$$

The conservation equations (Eqs.(1.14) - (1.20)) are numerically solved to yield the flow around immersed bodies.

Although the immersed boundary forcing $\mathbf{f}_{\mathrm{u}}$ ensures zero relative velocity at the particle-fluid interfaces, for periodic boundary conditions we need to ensure that the desired fluid-phase mean velocity will be attained. This is because unlike in inflow/outflow boundary conditions where the flow enters at a specified mass flow rate, there is no such mechanism for periodic boundary conditions. Therefore, in order to attain a desired fluid-phase mean velocity $\left\langle \mathbf{u}^{(f)} \right\rangle^d$, the mean pressure gradient $\left\langle \mathbf{g}_{\mathrm{IBM}} \right\rangle_{\mathcal{V}}$ is advanced in pseudo-time such that at the n^{th} time step it is given by

$$-\left\langle g_{\mathrm{IBM,\,i}} \right\rangle_{\mathcal{V}}^n = \rho_{\mathrm{f}} \frac{\left\langle u_i^{(f)} \right\rangle_{\mathcal{V}}^d - \left\langle u_i^{(f)} \right\rangle_{\mathcal{V}}^n}{\Delta t} + \frac{1}{(1-\varepsilon_{\mathrm{s}})\mathcal{V}} \left\{ -\oint_{\partial \mathcal{V}_{\mathrm{s}}} \psi^n n_i^{(s)} dA + \mu_{\mathrm{f}} \oint_{\partial \mathcal{V}_{\mathrm{s}}} \frac{\partial u_i^n}{\partial x_j} n_j^{(s)} dA \right\}, \tag{1.21}$$

where $\mathbf{g}' = \nabla \psi$, all quantities in the integrand are evaluated on the fluid side of the fluid-particle interface, and the superscript n implies the relevant quantities at the n^{th} time step. This equation for the volumetrically averaged pressure gradient is obtained by integrating the IBM momentum conservation equation (1.13) over the volume occupied by the fluid-phase. A finite difference approximation has been substituted for the unsteady term on right hand side of the above equation that drives the volume-averaged fluid velocity to its desired value. Since the immersed boundary force term is zero at grid nodes that lie outside the solid particles, the fluid-phase volume average of the immersed boundary force term $\left\langle I_f \mathbf{f}_u \right\rangle_{\mathcal{V}}$ is zero, thus resulting in zero contamination of the fluid pressure and velocity fields. The volume-averaged pressure gradient $\left\langle \mathbf{g}_{\mathrm{IBM}} \right\rangle_{\mathcal{V}}$ given by above equation, and the volume-averaged immersed boundary forcing term $\left\langle \mathbf{f}_{\mathrm{u}} \right\rangle_{\mathcal{V}}$ are used to evolve the volume-averaged velocity $\left\langle \mathbf{u} \right\rangle_{\mathcal{V}}$ by Eq. (1.17). For a statistically stationary flow, the equations are evolved in pseudo time until the average quantities reach a steady state, at which point the first term on the right hand side of Eq. (1.21) is negligible, and Eq. (1.21) reduces to the numerical counterpart of Eq. (1.11). This establishes that the resulting numerical solution to the IBM governing equations is a valid numerical solution to steady flow past homogeneous particle assemblies.

IBM with direct forcing was developed by Mohd-Yusof (Yusof, 1996) for his doctoral dissertation to solve for turbulent flow past a single particle. This code was subsequently completely rewritten by the Subramaniam research group at Iowa State University to implement the following improvements:

1. Modification of the forcing to remove the contamination in the fluid
2. Computation of drag for gas-solid suspensions at high volume fraction by establishing the connection with two-fluid theory and one-particle distribution function approaches

SIMULATION METHODOLOGY

We now describe how the physical parameters of the problem—mean flow Reynolds number and solid volume fraction—are specified in the simulation. For flow past homogeneous particle assemblies, a Reynolds number based on the magnitude of mean slip velocity between the two phases is defined as

$$\mathrm{Re}=\frac{U_{\mathrm{slip}}(1-\varepsilon_{\mathrm{s}})D}{\nu_{\mathrm{f}}}, \tag{1.22}$$

where $U_{\mathrm{slip}}=\left|\left\langle\mathbf{u}^{(f)}\right\rangle-\left\langle\mathbf{u}^{(s)}\right\rangle\right|$ is the magnitude of the mean slip velocity, D is the particle diameter, and $\left\langle\mathbf{u}^{(f)}\right\rangle$ and $\left\langle\mathbf{u}^{(s)}\right\rangle$ are the fluid-phase and solid-phase mean velocities, respectively.

The objective in direct numerical simulations is to solve the instantaneous mass and momentum conservation equations (Eqs. (1.12) and (1.13)) subject to the boundary conditions described earlier, in such a way that the resulting volumetric mean slip velocity corresponds to a desired Reynolds number. This system can be solved in three different ways, namely:

1. *Specified mean pressure gradient* $\langle\mathbf{g}\rangle$: In this method (Hill et al., 2001a; Hill, Koch, & Ladd, 2001c), a mean pressure gradient along with zero particle velocities are specified as inputs. As a result, the volumetric mean velocity evolves by Eq. (1.17) and the steady-state solution implies a Reynolds number. The drawback of this method is that Reynolds number cannot be specified as an input.

2a. *Specified solid-phase mean velocity* $\left\langle\mathbf{u}^{(s)}\right\rangle$: In this method the simulations are carried out in a laboratory frame of reference wherein the mean velocity $\langle\mathbf{u}\rangle$ is zero. Therefore, from Eq.(1.7), the desired fluid phase mean velocity $\left\langle\mathbf{u}^{(f)}\right\rangle=-\frac{\varepsilon_{\mathrm{s}}}{(1-\varepsilon_{\mathrm{s}})}\left\langle\mathbf{u}^{(s)}\right\rangle$. Substituting this expression for desired fluid-phase mean velocity $\left\langle\mathbf{u}^{(f)}\right\rangle$ in Eq. (1.22) results in an expression for $\left|\left\langle\mathbf{u}^{(s)}\right\rangle\right|$ in terms of the Reynolds number and other physical properties. In these simulations, the desired solid-phase mean velocity $\left|\left\langle\mathbf{u}^{(s)}\right\rangle\right|$ is attained by specifying equal velocities to all particles.

2b. *Specified fluid-phase mean velocity* $\left\langle\mathbf{u}^{(f)}\right\rangle$: In this method, particles are assigned zero velocity. Therefore, from Eq.(1.22), the desired fluid-phase mean velocity $\left\langle\mathbf{u}^{(f)}\right\rangle$ is known in terms of the input Reynolds number and other physical properties.

The advantage of methods 2a and 2b over the first method is that the desired Reynolds number can be specified as an input to the simulation, whereas it is an output in the first method. However, there is no relative advantage in choosing between the second and third methods. It is important to note that the velocity scale $\left(1-\varepsilon_s\right)U_{\text{slip}}$ is the correct scale to use for meaningful comparison of drag laws regardless of the simulation approach.

The solid volume fraction ε_{s} together with the ratio of computational box length to particle diameter L/D determines the number of solid particles N_{s} in the simulation:

$$N_{\text{s}} = \frac{6\varepsilon_{\text{s}}}{\pi}\left(\frac{L}{D}\right)^3 . \tag{1.23}$$

Numerical Parameters

The ratio of computational box length to particle diameter L/D, the number of solid particles N_{s} and the number of configurations/realizations $\mathcal{M}$ are numerical parameters of the simulation. Their influence on the numerical convergence of the IBM simulations is discussed in the following subsections.

The computational box is discretized using M grid cells in each direction, and this introduces a grid resolution parameter D_{m}. The number of grid cells is calculated as

$$M = \frac{L}{\Delta x} = \frac{L}{D}D_{\text{m}} , \tag{1.24}$$

where L is the length of the computational box, Δx is the size of each grid cell, and D_{m} is the number of grid cells across the diameter of a solid particle. The solution algorithm is advanced in pseudo-time from specified initial conditions to steady state using a time step Δt that is chosen as the minimum of the convective and diffusive time steps by the criterion

$$\Delta t = CFL \times \min\left\{\frac{\Delta x}{u_{\max}}, \frac{\Delta x^2(1-\varepsilon_{\text{s}})}{\nu_{\text{f}}}\right\}. \tag{1.25}$$

At the beginning of the simulation $u_{\max} = \left|\left\langle \mathbf{u}^{(f)} \right\rangle\right|$, and as the flow evolves the time step adapts itself to satisfy the above criterion.

Estimation of mean drag from simulations

Direct numerical simulation of flow through a particle assembly using the immersed boundary method results in velocity and pressure fields on a regular Cartesian grid. The drag force on the i^{th} particle, $\mathbf{F}_d^{(i)} = m^{(i)}\mathbf{A}^{(i)}$, is computed by integrating the viscous and pressure forces exerted by the fluid on the particle surface. The average drag force on particles in a homogeneous suspension for the μ^{th} realization is computed as

$$\left\{F_{d,j}\right\}_{\mathcal{V}}^{\mu}=\frac{1}{N_s}\sum_{i=1}^{N_s}m^{(i)}A_j^{(i)}=\frac{1}{N_s}\left\{-\left\langle g_{\mathrm{IBM},j}\right\rangle_{\mathcal{V}}\mathcal{V}_{\mathrm{s}}-\oint_{\partial\mathcal{V}_{\mathrm{s}}}\psi n_j^{(s)}dA+\mu_{\mathrm{f}}\oint_{\partial\mathcal{V}_{\mathrm{s}}}\frac{\partial u_j}{\partial x_k}n_k^{(s)}dA\right\},\quad(1.26)$$

which is obtained by integrating the pressure and viscous fields over the surface of each particle. In the last expression of the above equation, the first term is the force on all particles in the volume due to mean pressure gradient, the second term is the drag force due to the fluctuating pressure gradient field, and the third term is the viscous contribution to the drag force. This expression for the drag force is for one realization, and it is then averaged over $\mathcal{M}$ independent realizations in order to average over different particle configurations corresponding to the same solid volume fraction and pair correlation function. The ensemble-averaged drag is

$$\left\{F_{d,i}\right\}_{\mathcal{V},\mathcal{M}}=\frac{1}{\mathcal{M}}\sum_{\mu=1}^{\mathcal{M}}\left\{F_{d,i}\right\}_{\mathcal{V}}^{\mu},\quad(1.27)$$

which converges to the true expectation of the drag force $\left\langle\mathbf{F}_d\right\rangle$ (given by Eqs. (1.2) and (1.11)) in the limit $N_s\mathcal{M}\to\infty$. The ensemble-averaged drag force is later reported as a normalized average drag force F given by

$$F=\frac{\left|\left\{\mathbf{F}_d\right\}_{\mathcal{V},\mathcal{M}}\right|}{F_{\mathrm{Stokes}}},\quad(1.28)$$

where $F_{\mathrm{Stokes}}=3\pi\mu_{\mathrm{f}}DU_{\mathrm{slip}}(1-\varepsilon_{\mathrm{s}})$ is the Stokes drag.

Each numerical parameter must be chosen to ensure numerically converged, accurate, and physically meaningful results. Spatial and temporal discretization contribute to numerical error in the force on the i^{th} particle that scales as $O(\Delta x^p,\Delta t^q)$, where p and q depend on the order of accuracy of the method and the interpolation schemes at the particle boundary. For steady flow, the numerical error due to spatio-temporal discretization is solely determined by the spatial resolution parameter $\Delta x/D=1/D_{\mathrm{m}}$, which must be sufficiently small to ensure converged results. For the case where the particle positions are chosen to be randomly distributed, on each realization of the flow the computational domain should be chosen large enough so that the spatial auto-correlation in the particle force decays to zero. This guarantees that the periodic boundary condition does not introduce artificial effects due to interaction between the periodic images. For a given solid volume fraction ε_{s}, this determines a minimum value of $N_s=\lceil\varepsilon_{\mathrm{s}}V\rceil$. The number of multiple independent simulations $\mathcal{M}$ is determined by the requirement that the total number of samples $\sum_{\mu=1}^{\mathcal{M}}N_\mu$ in the estimate for the average force given by Eq.(1.26) be sufficiently large to ensure low statistical error.

Owing to the periodic lattice arrangement of particles in ordered arrays, it is sufficient to solve the flow for just one unit cell (i.e., one particle for the simple cubic (SC) lattice, and four particles for the face-centered cubic (FCC) lattice). For the special case of ordered arrays, since the number of particles is pre-determined, the ratio of computational box length to particle diameter L/D is not an independent numerical parameter. For ordered arrays the only numerical parameter is D_{m}, which determines the number of grid cells M required to resolve the flow.

Numerical Convergence

Here we establish that the IBM simulations result in numerically converged solutions. The test case chosen is steady flow past an ordered array of particles in a lattice arrangement, because for this case the only numerical parameter is the grid resolution D_m. Although we consider steady flows, we also verify that the time step chosen to evolve the flow in pseudo time from a uniform flow initial condition does not change the steady values of drag that we compute using IBM. For an FCC arrangement of particles ($\varepsilon_s = 0.2$, $\mathrm{Re} = 40$), Figure 3a shows the convergence of drag forces due to fluctuating pressure gradient (open symbols) and viscous stresses (filled symbols) as a function of grid resolution D_m for two different values of CFL number (0.2 denoted by squares and 0.05 denoted by triangles). Figure 3b shows the same convergence characteristics for a denser FCC arrangement with a solid volume fraction of 0.4 and $\mathrm{Re} = 40$. In both figures it can be seen that the IBM simulation result does not depend on the time step (CFL). With regard to spatial convergence, the figures show that the resolution requirements increase with increasing volume fraction. This is because higher local velocities are generated in the interstices between particles at higher solid volume fraction. While a minimum resolution of $D_m = 40$ is needed for converged results at $\varepsilon_s = 0.2$, the minimum resolution requirement increases to $D_m = 60$ for $\varepsilon_s = 0.4$. In addition to the dependence of grid resolution on volume fraction, increasing the mean flow Reynolds number also requires progressively higher grid resolution. Therefore, for the higher Reynolds number cases that are reported later, higher resolutions are used for the volume fractions 0.2 and 0.4, so that these cases are also adequately resolved.

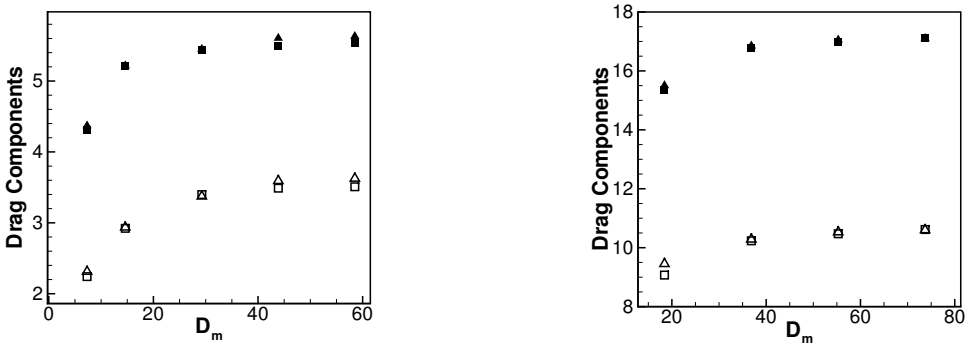

(a) *(b)*

Figure 3: Convergence characteristics of drag force with grid resolution D_m. The drag force contribution from fluctuating pressure gradient (open symbols) and viscous stresses (filled symbols) for FCC arrays (with grid resolution D_m) is shown for two CFL values of 0.2 (squares) and 0.05 (triangles). (a) Re=40, $\varepsilon_s = 0.2$; (b) Re=40, $\varepsilon_s = 0.4$.

When studying grid convergence of a numerical scheme it is sometimes useful to calculate the order of convergence that is implied by the numerical tests. However, the use of a regular Cartesian grid to solve for flow over spheres necessitates interpolation of pressure and viscous stresses from the grid to a finite number of particle surface points. For ordered arrays these interpolation errors cause the steady drag values to exhibit a weak dependence on the location of

the particle in the computational box (drag values can differ up to a maximum of 1%). Even for a fixed particle location in the computational box, the interpolation error depends on both the number of particle surface points and the grid resolution. These non-systematic interpolation errors preclude a reliable estimation of the order of convergence of the numerical scheme, which is formally at least second-order. Although the non-systematic interpolation errors prohibit the reliable quantification of spatial order of convergence, if a relative error is defined based on the solution at the finest grid, then a spatial order of convergence in the range 1.5-2 is obtained for the above cases. In other IBM studies (Ikeno & Kajishima, 2007), solution on a highly resolved unstructured grid is taken as a reference to compare the IBM solutions and convergence rates up to second order have been reported.

For the random arrays, in addition to errors arising from finite resolution, errors arise due to statistical fluctuations between different realizations and the box length is also an independent numerical parameter. Ideally, the effect of each numerical parameter on the numerical error should be investigated by varying that parameter while holding the other numerical parameters at fixed values. However, the choice of some numerical parameters must satisfy more than one requirement, and some error contributions are determined by the choice of more than one numerical parameter. Specifically, the choice of *L/D* is determined by more than one requirement (decay of spatial autocorrelation and the need for minimum number of samples in the average force estimate), and both *L/D* and the number of multiple independent simulations $\mathcal{M}$ determine the number of samples in the force estimate. These considerations as well as computational limitations did not permit the independent variation of numerical parameters. Therefore, a limited investigation of numerical parameter variation is presented here. To place this in context, we note that to our knowledge this is the most comprehensive study of numerical error and convergence for DNS of gas-solid flow.

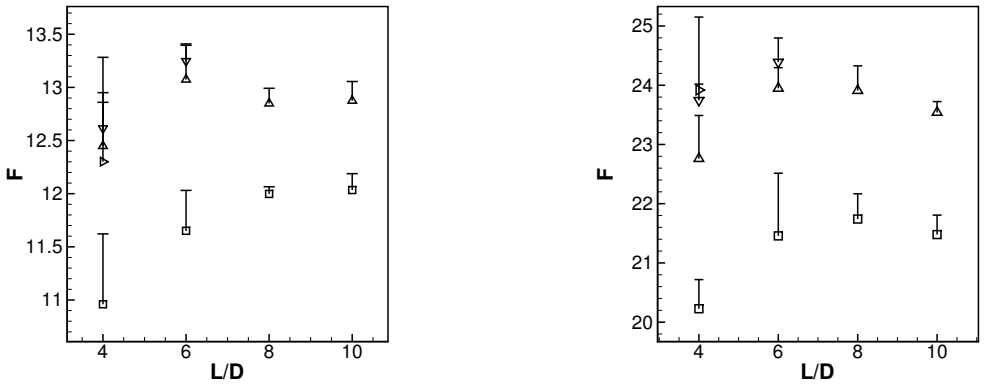

(a) *(b)*

Figure 4: Convergence characteristics of the normalized drag force with box length to particle diameter ratio L/D for random arrays at Re=20. Two solid volume fraction values are considered: (a) $\varepsilon_s = 0.3$*, (b)* $\varepsilon_s = 0.4$*. Four different values of* D_{m} *are shown: 10 (squares), 20 (upper triangles), 30 (lower triangles), and 40 (right triangles). Drag values have been averaged over 5 multiple independent simulations. Not all combinations of* D_{m} *and L/D are shown because with a serial code some combinations exceeded computational memory requirements.*

While for ordered arrays the box length and number of particles are determined by the volume fraction and type of lattice arrangement (SC/FCC), in random arrays these parameters have to be carefully chosen. If *L/D* is too small, then the spatial autocorrelations that are larger than the box size will not be captured and the periodic images will interact. For steady flow past random arrays ($\varepsilon_s = 0.3$, $\mathrm{Re} = 20$), Figure 4a shows the convergence characteristics of the normalized force with box length to particle diameter ratio *L/D* for four different values of D_m equal to 10 (squares), 20 (upper triangles), 30 (lower triangles), and 40 (right triangles). Figure 4b is the same comparison for a denser random arrangement with a volume fraction equal to 0.4. These results show that the drag value depends on *L/D* if the simulation is under-resolved, and the effect of grid resolution D_m is stronger than that of *L/D* for the cases considered here. Once the drag values are at their grid-converged values, there is no statistically significant dependence for *L>6D* in these cases. The simulations of flow past random arrays that are reported later in this work use higher resolutions when the Reynolds number exceeds 100, as shown in Table 1.

In summary, these numerical convergence test results show that the IBM simulations yield grid-independent results, and these results are also independent of the choice of time step used to advance the solution in pseudo time, provided the stability criterion is met. The tests for random arrays also show that the grid-converged results do not exhibit a statistically significant dependence on the computational box length for *L>6D*. However, these specific values for the numerical parameters should be treated as tentative because these limited set of tests cannot establish sharp limits on the minimum resolution required, and further numerical testing could refine these limits. A satisfactory number of MIS should ideally be determined by the determining the minimum number of samples for a given level of statistical error in the force estimate. However, this quantity is a strong function of Re and solid volume fraction. In the plots shown above, we have used 5 MIS for all the cases. While this results in a statistical error that is on the order of the other numerical error contributions, further testing is needed to refine this requirement. Clearly, the requirements of minimum *L/D*, minimum D_m, and minimum $\mathcal{M}$, together dictate a trade-off for a fixed level of computational work. Of these parameters, our tests reveal that the numerical error in IBM exhibits the highest sensitivity to grid resolution D_m. These numerical convergence tests provide useful guidelines in the choice of these parameters that approximately balance the error contributions, but further testing is needed for a complete error analysis.

VALIDATION TESTS

Isolated Sphere

The flow over an isolated sphere in an unbounded medium presents itself as the logical validation test for any direct numerical simulation approach to gas-solid flow. However, especially for simulations that use periodic boundary conditions, this turns out to be a difficult validation test. For simulations using periodic boundary conditions, flow through a very dilute simple cubic arrangement is taken as a close approximation to flow over an isolated sphere in an unbounded medium. Since the simple cubic lattice arrangement is not isotropic, it is known (Hill et al., 2001b) that the results for drag can depend on the orientation of the flow with respect to the unit vectors of the lattice for values of Reynolds number beyond the Stokes flow regime. In contrast,

there is of course no preferred direction for flow over an isolated sphere in an unbounded medium.

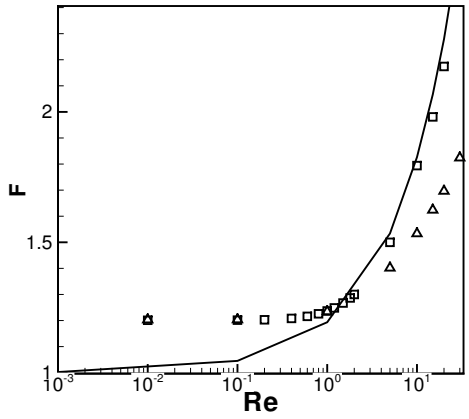

Figure 5: Normalized drag force F in a simple cubic array ($\varepsilon_s = 4.0 \times 10^{-4}$) as a function of Reynolds number and angle θ between the mean flow and the x- axis in the (x,y) plane. The symbols are from the IBM simulations: θ=0 (Δ), θ=π/16 (□). The solid line is the drag correlation for an isolated sphere in unbounded medium (Schiller & Naumann, 1933).

Figure 5 shows the comparison of the normalized drag force F in a simple cubic array ($\varepsilon_s = 4.0 \times 10^{-4}$) as a function of the Reynolds number from IBM simulations with a well-established correlation for an isolated particle in an unbounded medium (Schiller & Naumann, 1933). The drag computed for mean flow oriented at two different angles (θ=0 (Δ), θ=π/16 (□)) with respect to the lattice unit vector is shown to illustrate the dependence on flow angle. For Re<1 (in the Stokes regime), the normalized drag force is independent of the mean flow angle. However, the drag from IBM simulations is about 20% higher than the established correlation. The drag computed from IBM is within 4% of LBM simulations of dilute SC arrays using periodic boundary conditions. The interactions between the periodic images of the spheres result in higher drag values than an isolated sphere. It is expected that as the volume fraction is further reduced, the numerical predictions will get closer to the drag law in the Stokes limit. The sphere resolution D_m for the simulation shown is equal to 12.8 grid cells. Even more dilute simulations will require larger computational grids.

For Re>1, the IBM results are in good agreement with the existing drag law only when the mean flow is directed at an angle of π/16 in the (*x*, *y*) plane. This observation is consistent with the earlier LBM simulations (Hill et al., 2001b) where the authors argued that for mean flow angles close to 0 or π/4, the inertial contributions (or pressure gradient contributions) are reduced due to relatively larger wake interactions than for the case of θ=π/16. The lower inertial contributions result in a lower value for total drag for those flow angles. For Re<1 the normalized drag force value is independent of the mean flow angle because momentum transport is dominated by viscous diffusion. Since diffusion is symmetric about a sphere, the mean flow angle has no effect on the total drag force in the Stokes regime.

Stokes Flow

Several correlations have been proposed in the literature for the drag force in Stokes flow past ordered arrays (SC, FCC, BCC) of spheres. Different analytical and numerical techniques, such as analytical solution to the Stokes equations (Hasimoto, 1959), Galerkin methods (Snyder & Stewart, 1966; Sorensen & Stewart, 1974), and the boundary-integral method (Zick & Homsy, 1982), have been used to determine the drag force in Stokes flow past ordered arrays as a function of solid volume fraction. Since Zick and Homsy's results are within 6% of all the other studies, and include all three ordered configurations for the entire range of solid volume fraction, their values are used in as a benchmark to compare with IBM simulations. Figure 6 shows that the IBM simulations are in excellent agreement with reported values from dilute to close-packed limits.

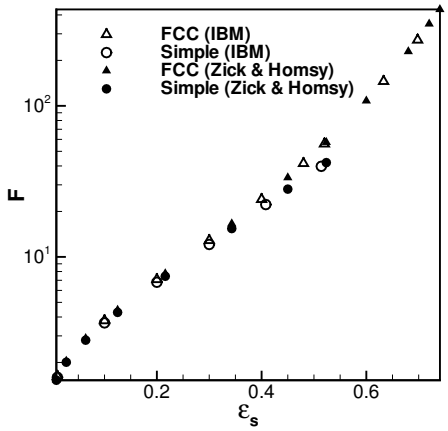

Figure 6: Comparison of the normalized drag force as a function of the solid volume fraction ε_s in in Stokes flow past simple cubic and FCC arrays from IBM simulations (open symbols) with the results of Zick & Homsy (filled symbols).

The grid resolution in the IBM simulations for the FCC cases is 25.24 grid points per particle diameter for the minimum volume fraction of 0.01, and 104 grid points per particle diameter for the maximum volume fraction of 0.698. For the simple cubic cases, D_m is equal to 40.08 for the minimum volume fraction of 0.01, and 149 for the maximum volume fraction of 0.514.

The validation tests described in this section show that the IBM simulations faithfully reproduce many standard results published in the literature. In cases where there are differences, these are within acceptable limits, and are mostly due to the higher resolution used in the IBM simulations. Having established that the IBM simulations are numerically convergent and having validated them in standard tests, we now use IBM to study drag in steady flow past ordered and random arrays.

ORDERED ARRAYS

Ladd (Ladd, 1994b) and Hill et al. (Hill et al., 2001b) have studied steady flow past ordered arrays of particles using LBM simulations. Our purpose in revisiting this problem is two-fold. IBM simulations of flow past ordered arrays serve to further validate the method for cases where we can compare with published data of Hill et al. Secondly, we have more comprehensively

explored the parameter space defined by (Re , ε_s), especially the low volume fraction region, with higher numerical resolution than reported thus far in the literature. The dilute cases are more computationally demanding, and have therefore not received as much attention. However, the behavior of the drag force in the dilute limit is important because it defines a limiting behavior that drag correlations are typically constrained to satisfy. Our IBM simulations in the dilute regime reveal some new insights into the correct limiting behavior that should be imposed as a constraint on drag correlations.

Figure 7 shows the behavior of the normalized drag force obtained from IBM simulations (open symbols) for steady flow past a SC arrangement of particles as a function of Reynolds number, for volume fractions ranging from very dilute to close-packed limits. Also shown in the same figure is the comparison (wherever the data is available) with the LBM simulations (filled symbols) of HKL. Figure 8 shows the same comparison for the FCC arrangement. As both figures show, the IBM and LBM simulations are in excellent agreement. These results serve to further validate the use of IBM for simulation of flow past homogeneous particle assemblies.

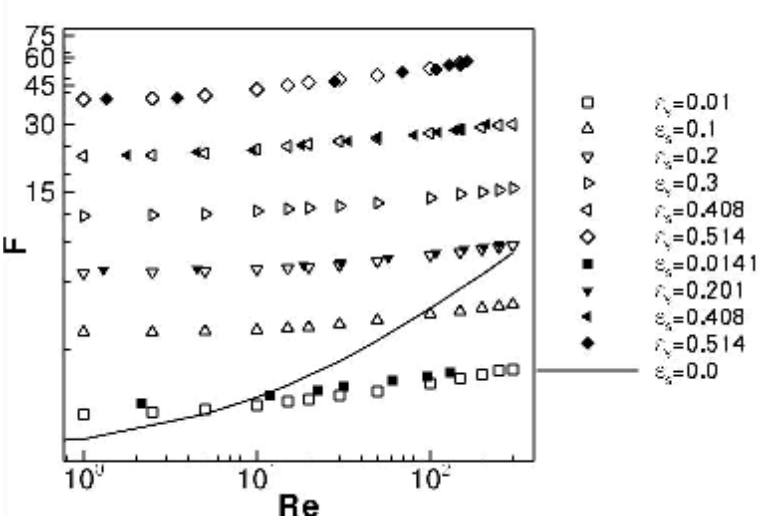

Figure 7: Comparison of the normalized drag force F for SC arrangement obtained from IBM (open symbols) with the LBM simulations (filled symbols) of HKL. The solid line is the drag law for a single particle in an unbounded medium. The flow is directed along the x- axis.

The solid line in Figures 7 and 8 is the drag on a single particle in an unbounded medium from the Schiller and Naumann correlation. Comparison with the single sphere drag law (solid line) reveals that for moderate to high Reynolds numbers, the dilute volume fractions in ordered arrays experience lesser drag than the drag on a single particle. As observed earlier for the dilute SC array (see and its discussion), and also studied comprehensively in HKL, the normalized drag force in ordered arrays is a function of the flow angle. Therefore, in order to avoid the additional parametrization of the problem by flow angle, all the simulations have been performed for the case where the mean flow is directed along the x- axis. However, as shown in HKL, a change in the flow angle can result in drag values that differ by as much as 200-300% from the zero flow angle case. The main conclusion to be drawn from these simulations is that the single sphere drag law is not the asymptotic limit of the dilute ordered arrays data. As we shall see in the next

section, the same is true for random arrays also, although they do not exhibit the strong dependence on flow angle characteristic of ordered arrays.

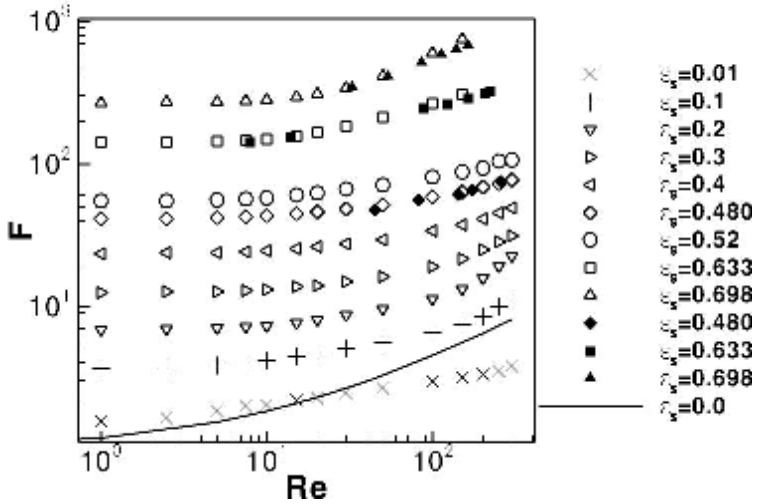

Figure 8: Comparison of the normalized drag force F for FCC arrangement obtained from IBM (open symbols) and with the LBM simulations (filled symbols) of HKL. The solid line is the drag law for a single particle in an unbounded medium. Flow is directed along the x- axis.

RANDOM ARRAYS

Fixed assemblies of randomly distributed particles are closer to the freely evolving suspension problem that we seek to model than ordered arrays. The particle positions are initialized by first allowing them to evolve to an equilibrium state following elastic hard-sphere collisions.

We have performed IBM simulations with numerical resolutions comparable or higher than those used in HKL and BVK, again with an emphasis on characterizing the dilute limit, which is used to as a limiting case constraint to determine drag law coefficients. Later in this section, the numerical parameters used in the current IBM simulations are compared with those used in the LBM simulations of HKL and BVK. In the following, the principal IBM results and the underlying physical mechanisms they reveal are discussed. Implications of the results for drag laws are then summarized.

Dilute Arrays

Figure 9 shows the dependence of normalized drag force on the Reynolds number for a random configuration at a dilute volume fraction of 0.01. Symbols are the IBM simulations, with square symbols for the mean flow directed along the *x*- axis, and triangles for the mean flow directed at an angle of $\pi/16$ in the *x*-*y* plane. Solid and dashed-dot lines are the monodisperse drag laws from LBM simulations of HKL and BVK, respectively, and the dashed line is the single sphere drag law of Schiller and Naumann.

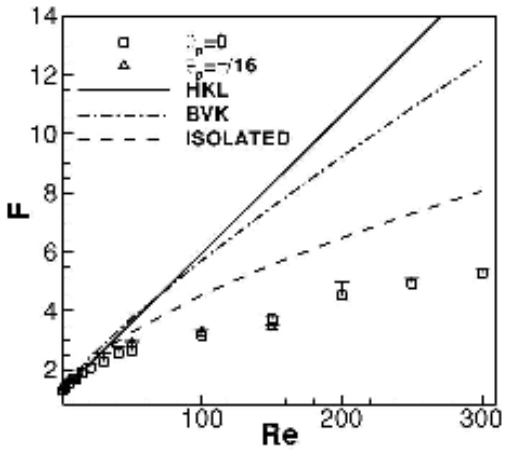

Figure 9: Normalized drag force F vs Reynolds number for a random arrangement of particles at solid volume fraction equal to 0.01. Symbols are the IBM simulations: squares denote the case where the flow is directed along the x- axis; triangles denote the case where the flow is directed at an angle of $\pi/16$ *in the x-y plane.*

Comparison of the IBM simulations with existing monodisperse drag laws of HKL and BVK shows an excellent match in the Stokes regime and at low Re, but differences as high as 100-200% in the moderate and high Re regime. HKL (Hill et al., 2001a) simulated such dilute volume fractions only for the Stokes regime, but due to the coarse resolution of less than 2 lattice nodes for particle diameter they did not simulate higher Reynolds numbers for this volume fraction. BVK did not simulate any case for $\varepsilon_s \le 0.1$. In HKL it is noted that due to the approximate approach used to obtain the inertial contribution (denoted by F_3 in their study) to the total drag, their drag law is a good estimate of the actual drag force over the entire range of Reynolds number only for relatively high solid volume fractions. This is a plausible explanation for the departure of IBM simulations from the HKL drag law. The departure of IBM simulations from BVK's monodisperse drag law is attributed to the incorrect constraint imposed on their drag law to the single-sphere drag correlation at infinite dilution. The BVK drag law assumes that the drag in random homogeneous suspensions at infinite dilution (i.e., $\varepsilon_s \to 0$) should tend to the drag on an isolated particle. From both IBM and LBM simulations, it is clear that this assumption does not hold true even at the moderately dilute volume fraction of 0.01.

At low Re, viscous terms that are local (short range) dominate. Since the viscous forces are short ranged, it is reasonable to expect that at infinite dilution and low Re, the normalized drag force will approach that of single-sphere drag (i.e., $F \to 1$ as $\varepsilon_s \to 0$ and $\mathrm{Re} \to 0$). As the Reynolds number increases, the contribution from inertial terms dominates the viscous effects, and since pressure obeys an elliptic equation these are long range (nonlocal) interactions. For moderate to high Reynolds numbers flow past random arrays, even for fairly dilute solid volume fractions the simulation data do not support the assumption of constraining the drag law to approach that of single-sphere.

Similar to the observations for ordered arrays (Figures 7 and 8), the drag force on dilute suspensions for moderate to high Reynolds numbers is less than the drag force experienced by an isolated particle in an unbounded medium. However, unlike in ordered arrays the drag force in

random arrays is not dependent on the flow angle due to isotropy of the particle configuration. For ordered arrays, the strong influence of flow angle on the drag force at moderate to high Reynolds numbers is attributed by HKL to the different length scales at which the inertial contributions interact. The distribution of neighbor particles in ordered arrays is anisotropic, and the pair correlation function is sharply peaked at the lattice points. However, in the random particle configurations generated by elastic hard-sphere collisions, the pair correlation is isotropic. Therefore, the drag force is insensitive to flow angle for all Reynolds numbers in random arrays.

Moderately Dilute to Dense Arrays

Figure 10 shows the comparison of normalized drag force in random arrays for volume fractions equal to 0.1 and 0.2 obtained from IBM simulations (open symbols) with the existing monodisperse drag laws of HKL and BVK. shows the same comparison for volume fractions equal to 0.3 and 0.4. It can be seen that IBM simulations are in excellent agreement with HKL's drag law for Re up to 100, which is nearly the upper limit of Reynolds number simulated by HKL. The extension of their drag law to higher Re does not agree well with IBM simulations as the solid volume fraction is reduced. This is attributed to the observation made in HKL that their drag law is a good estimate of the actual drag force over a wide range of Reynolds number only for relatively high solid volume fractions.

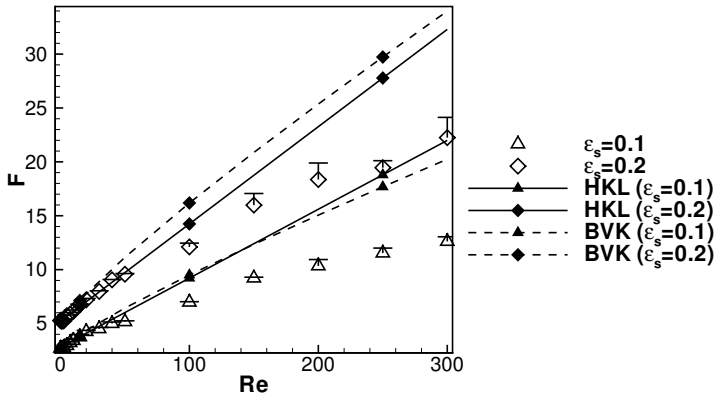

Figure 10: Comparison of the normalized drag force F for random arrays at volume fractions equal to 0.1 and 0.2 from IBM simulations (open symbols) with the monodisperse drag laws of HKL and BVK.

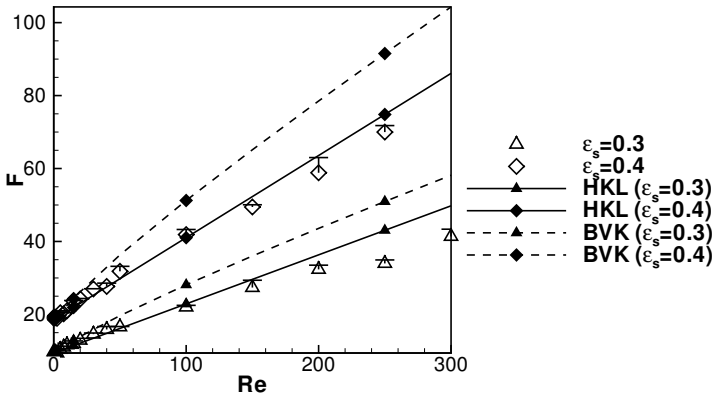

Figure 11: Comparison of the normalized drag force F for random arrays at volume fractions equal to 0.3 and 0.4 from IBM simulations (open symbols) with the monodisperse drag laws of HKL and BVK.

Numerical Parameters and Resolution

Choosing the numerical resolution for random arrays or a fixed level of computational work should be based on an optimal combination of box-size and grid resolution. Table 1 compares the numerical resolutions for different volume fractions used in our IBM simulations with those used in LBM simulations of HKL and BVK. It is noted that not all choices of the numerical parameters for IBM are in the "resolved" range as determined by our limited set of numerical convergence tests. However, as noted earlier, these tests are themselves not comprehensive, and so ultimately the choice of numerical parameters reflects an attempt to balance various contributions to the numerical error. Given the relatively low sensitivity of the mean drag force to *L/D* ratio in IBM, we have used values from past LBM simulations as a guideline, choosing higher grid resolution over larger box size in some of our IBM simulations.

The numerical resolutions for HKL that are reported in Table 1 are those used for the maximum Reynolds numbers and are taken from Table 1 in (Hill et al., 2001b). For Stokes flow, HKL have used similar numerical resolution for $\varepsilon_s \geq 0.1$. However, for very dilute volume fractions, very coarse resolutions of less than 2 lattice nodes across a particle diameter have been used. In BVK, a constant resolution of 17.5 lattice units across a particle diameter was used for $\varepsilon_s \leq 0.2$, and for higher volume fractions, their results were obtained by averaging over two resolutions of 17.5 and 25.5 lattice units. Therefore, in Table 1, we have used the average value of 21.5 lattice units to report their resolutions for $\varepsilon_s \geq 0.3$. In both the studies, random configurations for volume fraction less than 0.1 were not simulated for the entire range of Reynolds numbers. So there is no numerical resolution comparison for $\varepsilon_s = 0.01$. Table 1 shows that the IBM simulations are consistently better resolved in terms of the number of particles, grid resolution, and the box-size. BVK performed greater number of MIS but the scatter in IBM data does not point to a need for such high number of MIS. Therefore, normalized drag values averaged over 5 MIS are reported here.

ε_s		N_s		$\mathcal{M}$	D_m		L/D	
		Re < 100	Re > 100		Re < 100	Re > 100	Re < 100	Re > 100
0.01	HKL	-			-		-	
	BVK	-			-		-	
	IBM	64	13	5	10	20	15	9
0.1	HKL	16		5	9.6		4.38	
	BVK	54		20	17.5		6.6	
	IBM	80	41	5	20	30	7.5	6
0.2	HKL	16		5	17.6		3.47	
	BVK	54		20	17.5		5.2	
	IBM	161	34	5	20	40	7.5	4.5
0.3	HKL	16		5	17.6		3.06	
	BVK	54		20	21.5		3.07	
	IBM	71	26	5	30	50	5	3.6
0.4	HKL	16		5	33.6		2.73	
	BVK	54		20	21.5		4.13	
	IBM	95	20	5	30	60	5	3

Table 1: Comparison of the numerical resolutions used for random arrays in IBM simulations with the past LBM simulations of HKL and BVK. For each entry, first and second rows correspond, respectively, to the LBM simulations of HKL and BVK, and the third row corresponds to the current IBM simulations. For the IBM simulations, different numerical parameters are used for $\mathrm{Re} \le 100$ *and* $\mathrm{Re} > 100$. *These are shown in two separate columns.*

Computational Cost

The computational cost associated with IBM simulations of flow past fixed assemblies of monodisperse particles performed using a serial code is discussed in this section. All the simulations are performed on an AMD Opteron cluster with 148 compute nodes. The compute nodes consist of 2.4 GHz dual core dual processors. The processor type is AMD 2800 Opteron with a peak performance of 4.8 Gigaflops.

At a given volume fraction and Reynolds number, the simulation time for the mean particle drag to reach steady state is denoted $\mathrm{T}_{\mathrm{sim}}$ and can be written as:

$$\mathrm{T}_{\mathrm{sim}} = \hat{\mathrm{T}}\left(\varepsilon_s\right) \times M\left(\mathrm{Re}, \varepsilon_s\right) \times N_{\mathrm{T}}\left(\mathrm{Re}, \varepsilon_s\right).$$

In the above equation, $\hat{\mathrm{T}}$ is the computational cost per grid cell per time step, M denotes the number of grid cells and N_{T} is the number of time steps taken for the mean drag to reach a steady state.

The computational cost per grid cell per time step $\hat{\mathrm{T}}$ is independent of the Reynolds number and depends only on the volume fraction. In Table 2, the values for $\hat{\mathrm{T}}$ are reported in microseconds for various volume fractions. It can be seen from Table 2 that $\hat{\mathrm{T}}$ increases with volume fraction. The number of grid cells M required for a well resolved simulation also depends on the volume

fraction and Reynolds number as shown in Table 1. From the values of optimal L/D and D_m given in Table 1, the number of grid cells can be calculated using:

$$M = \left(\frac{L}{D} D_m \right)^3 .$$

It should be noted that the number of time steps N_T that is required for the average drag on the particles to reach a steady state also depends on the physical parameters of the problem (solid volume fraction and Reynolds number). Typically, it is observed that at a given Reynolds number, dilute particle assemblies take more time to attain steady state than the denser ones. And at a given volume fraction, suspensions at higher Reynolds numbers take longer to attain steady state.

ε_s	$\hat{T}$ (μS)
0.01	4.612
0.1	5.033
0.2	5.693
0.3	5.745
0.4	6.071

Table 2: Computational cost per grid cell per time step for IBM simulations of flow past fixed assemblies of monodisperse particles at various volume fractions.

Summary

IBM simulations show an excellent match with the drag correlations proposed by HKL and BVK for low Reynolds number for both dilute and moderately dense random arrays. However, the IBM simulations show a significant departure from these correlations at higher Re, and for dilute cases. The drag law proposed by HKL is stated to be more reliable for all Reynolds numbers only at higher volume fraction. The BVK drag correlation is proposed based on a fit to 5 drag values over a wide range of Reynolds number, and their simulations appear to be susceptible to numerical resolution errors. For a given volume fraction, they used a constant resolution of the particle diameter to simulate Reynolds numbers ranging from 21 to 1000. As the volume fraction is increased, the number of grid/lattice nodes in the gaps between the spheres decrease and a progressively higher grid resolution is required. In the HKL study the particle resolution was increased from 9.6 lattice units per particle diameter for the lowest volume fraction of 0.1 to 41.6 lattice units for the highest volume fraction of 0.641, which is a four-fold increase. However, in the BVK study the particle resolution increased by only a fraction for a wide volume fraction range of 0.1-0.6. The IBM simulations suggest that a more complete parametric study at high resolution could significantly revise these existing drag laws.

ASSESSMENT OF IBM FOR DRAG LAW FORMULATION

Simulations of steady flow past homogeneous particle assemblies using IBM reveal that fundamentally differing computational approaches to gas-solids flow are in remarkably good agreement for a wide variety of test cases. Overall this is strong evidence of the consistency

between different computational approaches to the problem of drag law formulation in gas-solids flow, which is difficult to study through experiment. However, all computational predictions of drag in gas-solids flow are subject to uncertainties arising from numerical error, and should be interpreted as accurate only within 5%. In the following we compare and contrast the IBM approach with LBM, which is a popular computational approach for gas-solids flow.

While IBM solves the continuum Navier-Stokes equations, LBM solves for the discrete one-particle velocity distribution function whose evolution is described by the lattice Boltzmann equation (He & Luo, 1997). It is useful to think of LBM as a solution to the lattice Boltzmann equation, which is obtained by Hermite-Gauss quadrature of the modeled Boltzmann equation. LBM fundamentally differs from continuum solutions to Navier-Stokes equations like IBM because it directly solves for a discrete form of the velocity distribution function at the molecular level. From the LBM solution the hydrodynamic mean fields such as fluid velocity and pressure can be calculated. Since LBM operations are local in physical space, it avoids solving the elliptic pressure Poisson equation that is needed in incompressible continuum flow solvers. This paves way for efficient parallelization of LBM, which has opened door to solving realistic flow problems (Chen & Doolen, 1998).

However, there are some issues worth considering when using LBM for gas-solids suspension. The restriction of molecular velocities to discrete values on a lattice is now known to be unnecessary, and even undesirable for many flow problems, especially in multiphase flow (Fox, 2008). Another feature of LBM is that it always results in a compressible flow solution, and as a result the solution of incompressible flow at high Reynolds numbers is challenging. In order to reduce the errors due to compressibility effects at higher Reynolds numbers, the viscosity of the fluid has to be reduced (Ladd, 1994a, 1994b).

When we consider suspension flows, some very important differences arise between IBM and LBM. In LBM a spherical particle is represented by a stair-step lattice approximation, i.e., the surface is represented by a set of lattice sites closest to the input diameter D_0. Due to this stair-step representation of the particle surface, the exact value of the particle diameter that appears in the LBM drag law is not specified *a priori*. Furthermore, the bounce-back scheme used to implement the no slip boundary condition at the particle-fluid interface does not result in a zero velocity contour coincident with a stationary sphere boundary. Therefore, in LBM the drag computed directly from the fluid stress at the particle surface does not correspond to the drag on a sphere of diameter D_0. The drag values in LBM simulations are assumed to correspond to an effective hydrodynamic diameter D_h that is unknown *a priori*. The hydrodynamic diameter D_h is obtained *a posteriori* by calibrating the LBM simulations against the analytical solution of Hasimoto (Hasimoto, 1959) for Stokes flow in a dilute SC arrangement of spheres. This hydrodynamic diameter depends on the fluid viscosity as well as the particle size. Therefore, a calibration curve is needed in LBM for every choice of kinematic viscosity and particle diameter D_0. This is a serious limitation for a DNS calculation. In contrast, in IBM the particle surface is represented as a sphere. The fluid stress on the particle surface is calculated directly from the flow fields with no intermediate calibration procedure. Therefore, IBM is a first-principles, physics-based true DNS approach for simulation of gas-solid flows.

It is also interesting to note that the drag on the particle reported using D_0 gives first order convergence whereas drag reported using D_h results in approximately quadratic convergence (Ladd & Verberg, 2001). However, this convergence rate is not independent of the kinematic viscosity of the fluid. Even though the calibration of hydrodynamic diameter is only done for a single sphere, the same calibration is used for simulating dense ordered suspensions in the Stokes regime (Ladd, 1994a, 1994b) as well as random arrays at higher Reynolds number (Hill et al., 2001a; van der Hoef et al., 2005).

LBM is a highly efficient and robust solution methodology for gas-solids flow. Overall, it appears that LBM results for mean drag are relatively insensitive to grid resolution when compared with IBM. However, this insensitivity of the LBM solution to grid resolution should be carefully interpreted because LBM yields stable solutions even when the flow is highly under-resolved. For instance, (Beetstra et al., 2007) show that the drag force for a dense random packing of 0.5 at Reynolds number equal to 1049 is insensitive to the grid resolution in the range 10 to 50 lattice units per particle diameter. However, for these grid resolutions it is clear that the boundary layers around the particles cannot be resolved at such a high Reynolds number. Some studies also report greater sensitivity of LBM to grid resolution. For example, in the monodisperse simulations of (van der Hoef et al., 2005) at a volume fraction of 0.5 in the Stokes flow regime, a strong dependence of the drag force on the grid resolution and kinematic viscosity is observed.

The sensitivity of IBM results to grid resolution has already been discussed, and we find that the IBM results for the surface viscous stress show the correct increasing trend with increasing grid resolution as the velocity gradients are better resolved. If IBM is used to simulate high Reynolds number flows with insufficient resolution (e.g., Re>500 with grid resolution in Table 1), the solution becomes unstable because of the non-dissipative second-order upwind schemes that have been incorporated for high accuracy. This informs the IBM user that higher grid resolution should be employed to obtain stable and accurate solutions.

From the preceding discussion we can see that IBM has some unique advantages in solving gas-solids flow problems that derive from its solution approach to the continuum Navier-Stokes equations. By virtue of its implementation into structured Cartesian grid solvers, it incurs minimal increase in computational cost with increasing number of particles. To give a rough idea of the order of magnitude of the increase in computational cost, the increase is only about 25% going from 2 particles to 97 particles, but the exact value depends on the Reynolds number and volume fraction. The results presented in this chapter show that IBM yields numerically convergent solutions to important hydrodynamic problems in gas-solids flow, which compare well with many established results in the literature. We also find that this powerful tool is capable of giving additional insight into the important limiting case of steady flow past dilute random arrays. Also a more thorough exploration of the volume fraction-Reynolds number parameter space suggests significant changes to existing drag correlations may be required. In the next section we outline future directions for IBM as a computational method for solving gas-solids flow problems.

FUTURE DIRECTIONS

Future directions for the use of IBM as a DNS approach for gas-solids flow can be classified into two broad categories: (i) applications of the IBM approach described in this work to other gas-solids flow problems, and (ii) development of the IBM formulation for other gas-solids flow problems.

Other applications of the IBM approach

The IBM approach described in this work can be used to quantify the terms that appear in the second moment equations that derive from the transport equation of the one-particle distribution function (Eq. (1.1)). Preliminary work in this direction is already in progress, and our initial studies indicate that such calculations will require the simulation of freely moving suspensions. In these calculations the particles need to evolve by the hydrodynamic force that the fluid exerts through pressure and surface viscous stresses. Particle collisions also need to be accounted for, and for dense suspensions it is appropriate to use the discrete element method based on the spring-dashpot soft-sphere model (Cundall & Strack, 1979).

In gas-solids suspension flows, the problem of segregation of unlike particles (differing in size or density) is of great practical interest. The IBM approach described here can be easily extended to simulate polydisperse assemblies of particles, and work is ongoing to quantify drag laws for polydisperse gas-solids flow using IBM.

It is well established in the literature that gas-solids riser flows exhibit particle clustering effects (Collins & Keswani, 2004; Heynderickx, Das, De Wilde, & Marin, 2004; Knowlton, Karri, & Issangya, 2005; Krol, Pekediz, & de Lasa, 2000; Wylie & Koch, 2000). Also experiments (Moran & Glicksman, 2003) have shown that gas-phase turbulence interacts differently with particle clusters, than with individual particles. The IBM method described here has been modified to simulate an inflow-outflow boundary condition to study the influence of different particle arrangements (uniform and clustered) on upstream gas-phase turbulence (Xu, 2008). It should be mentioned that the current computational power only allows for DNS of simple flows, such as flow past homogeneous assemblies considered in this study. Application of DNS to device scale problems is not envisaged because of the high computational cost arising from the large range of scales.

Extensions to the current IBM formulation

The principal extensions to the IBM formulation lie in the areas of (a) generalizing boundary conditions, (b) extending the equation set to include other physical effects, such as transport of chemical species and heat transfer, and (c) improving the solution procedure. The IBM approach described here can be generalized to incorporate arbitrary boundary conditions and to include complex geometries.

The transport of scalars, such as chemical species or temperature, in gas-solids flow is also a problem of practical importance. The IBM approach can be applied to the problem of transport of a passive scalar by a relatively easy augmentation of the existing equation set. This extension is also in progress and preliminary results show that IBM is a versatile tool that can be used to study heat and mass transfer in gas-solids flow as well.

The solution procedure employed in this work can be improved by incorporating recent advances in differencing the pressure equation that have been derived in the context of immersed interface methods. This differencing formula accounts for a discontinuous jump in the pressure across the solid-fluid interface (Xu & Wang, 2006, 2008 and Lee & Leveque, 2003).

Parallelization strategy

A major advantage of the immersed boundary method is its capability to solve for flow over complex geometries on a uniform Cartesian grid. Efficient domain decomposition algorithms for Cartesian topologies are provided in almost all the standard MPI implementations – an advantage of Cartesian topologies compared to body-fitted meshes where one has to rely on third-party libraries like METIS for domain decomposition. The dominant communication costs in any parallel implementation depend upon the order of accuracy of the discretization schemes. For example, a second-order central differencing scheme requires communication of the solution on the first layer of grid nodes that lie adjacent to the partition boundaries. In the parallel implementation of IBM, no special distribution of the particles among the processors is required as the particles are assigned to processors based on their spatial locations. A particle that lies on a partition boundary is partitioned appropriately and the velocity and pressure fields that are exchanged after every time step are sufficient to calculate the immersed boundary force acting on the portion of the particle that lies within a processor. The immersed boundary field is communicated at each time step similar to communications for pressure and velocity fields. Therefore, as discussed before, the parallel implementation preserves the scale up of computational cost with the number of particles as the communication overhead incurred for forcing field is minimal.

CONCLUSION

IBM is a powerful and efficient computational method for direct numerical simulation of gas-solids flow. This contribution connects the quantities computed from DNS using the IBM approach with the interphase momentum transfer term arising in theoretical approaches to gas-solids flow. This correspondence is described at different levels, starting from the one-particle distribution function and leading naturally to the averaged equation in that approach. An important connection of IBM quantities with two-fluid theory is also established. The numerical convergence of IBM is established and its performance in various validation tests is described. It is shown that IBM simulations reproduce known results for the average drag in Stokes flow past ordered arrays. For random arrays, the IBM results reveal interesting insights in the dilute limit, and suggest changes to existing drag laws may be required following comprehensive exploration of the Reynolds number-solid volume fraction parameter space. The IBM approach is versatile, and can be extended to include effects of gas-phase turbulence, polydispersity in the size distribution of solid particles, and transport of chemical species and heat due to fluid flow.

ACKNOWLEDGMENTS

This work is supported in part by the National Energy Technology Laboratory through Ames Laboratory grant DE-AC02-07CH11358 (RG and SS) and DOE-AR grant DE-FC26-07NT43098

(RG, ST, and SS). The authors would like to thank Dr. M. G. Pai for insightful discussions during the course of this study, and useful comments on a draft of the manuscript .

REFERENCES

Beetstra, R., van der Hoef, M. A., & Kuipers, J. A. M. (2007). Drag force of intermediate Reynolds number flow past mono- and bidisperse arrays of spheres. *Aiche Journal, 53*(2), 489-501.

Chapman, S., & Cowling, T. G. (1952). *The mathematical theory of non-uniform gases; an account of the kinetic theory of viscosity, thermal conduction, and diffusion in gases* ([2d ed.). Cambridge [Eng.]: University Press.

Chen, S., & Doolen, G. D. (1998). Lattice Boltzmann method for fluid flows. *Annual Review of Fluid Mechanics, 30*, 329-364.

Collins, L. R., & Keswani, A. (2004). Reynolds number scaling of particle clustering in turbulent aerosols. *New Journal of Physics, 6*, -.

Cundall, P. A., & Strack, O. D. L. (1979). Discrete Numerical-Model for Granular Assemblies. *Geotechnique, 29*(1), 47-65.

Drew, D. A., & Passman, S. L. (1999). *Theory of multicomponent fluids*. New York: Springer.

Fox, R. O. (2008). A quadrature-based third-order moment method for dilute gas-particle flows. *Journal of Computational Physics, 227*(12), 6313-6350.

Garzo, V., Hrenya, C. M., & Dufty, J. W. (2007). Enskog theory for polydisperse granular mixtures. II. Sonine polynomial approximation. *Physical Review E, 76*(3), -.

Goldstein, D., Handler, R., & Sirovich, L. (1993). Modeling a no-slip flow boundary with an external force field. *Journal of Computational Physics, 105*(2), 354--366.

Hasimoto, H. (1959). On the periodic fundamental solutions of the Stokes equations and their application to viscous flow past a cubic array of spheres. *J. Fluid Mech., 5*(2), 317-328.

He, X. Y., & Luo, L. S. (1997). Theory of the lattice Boltzmann method: From the Boltzmann equation to the lattice Boltzmann equation. *Physical Review E, 56*(6), 6811-6817.

Heynderickx, G. J., Das, A. K., De Wilde, J., & Marin, G. B. (2004). Effect of clustering on gas-solid drag in dilute two-phase flow. *Industrial & Engineering Chemistry Research, 43*(16), 4635-4646.

Hill, R. J., Koch, D. L., & Ladd, A. J. C. (2001a). The first effects of fluid inertia on flows in ordered and random arrays of spheres. *J. Fluid Mech., 448*(213-241).

Hill, R. J., Koch, D. L., & Ladd, A. J. C. (2001b). Moderate-Reynolds-number flows in ordered and random arrays of spheres. *Journal of Fluid Mechanics, 448*, 243-278.

Hill, R. J., Koch, D. L., & Ladd, A. J. C. (2001c). Moderate Reynolds number flows in ordered and random arrays of spheres. *J. Fluid Mech., 448*(243-278).

Ikeno, T., & Kajishima, T. (2007). Finite-difference immersed boundary method consistent with wall conditions for incompressible turbulent flow simulations. *Journal of Computational Physics, 226*(2), 1485-1508.

Jenkins, J. T. (1998). Kinetic theory for nearly elastic spheres. *Physics of Dry Granular Media, 350*, 353-370.

Knowlton, T. M., Karri, S. B. R., & Issangya, A. (2005). Scale-up of fluidized-bed hydrodynamics. *Powder Technology, 150*(2), 72-77.

Koch, D. L. (1990). Kinetic-Theory for a Monodisperse Gas-Solid Suspension. *Physics of Fluids A-Fluid Dynamics, 2*(10), 1711-1723.

Koch, D. L., & Hill, R. J. (2001). Inertial effects in suspension and porous-media flows. *Annual Review of Fluid Mechanics, 33*, 619-647.

Krol, S., Pekediz, A., & de Lasa, H. (2000). Particle clustering in down flow reactors. *Powder Technology, 108*(1), 6-20.

Ladd, A. J. C. (1994a). Numerical Simulations of Particulate Suspensions Via a Discretized Boltzmann-Equation .1. Theoretical Foundation. *Journal of Fluid Mechanics, 271*, 285-309.

Ladd, A. J. C. (1994b). Numerical Simulations of Particulate Suspensions Via a Discretized Boltzmann-Equation .2. Numerical Results. *Journal of Fluid Mechanics, 271*, 311-339.

Ladd, A. J. C., & Verberg, R. (2001). Lattice-Boltzmann simulations of particle-fluid suspensions. *Journal of Statistical Physics, 104*(5-6), 1191-1251.

Lee, L., & Leveque, R. J. (2003). An immersed interface method for incompressible Navier-Stokes equations. *Siam Journal on Scientific Computing, 25*(3), 832-856.

Liboff, R. L. (1990). *Kinetic theory : classical, quantum, and relativistic descriptions*. Englewood Cliffs, N.J.: Prentice Hall.

Mohd-Yusof, J. (1996). *Interaction of massive particles with turbulence.* Cornell University.

Moran, J. C., & Glicksman, L. R. (2003). Experimental and numerical studies on the gas flow surrounding a single cluster applied to a circulating fluidized bed. *Chemical Engineering Science, 58*(9), 1879-1886.

Pai, M. G., & Subramaniam, S. (2009). A comprehensive probability density function formalism for multiphase flows. *Journal of Fluid Mechanics, Accepted, In Press*.

Peskin, C. S. (1982). The Fluid-Dynamics of Heart-Valves - Experimental, Theoretical, and Computational Methods. *Annual Review of Fluid Mechanics, 14*, 235-259.

Pope, S. B. (2000). *Turbulent Flows*. Cambridge: Cambridge University Press.

Rai, M. M., Gatski, T. B., & Erlebacher, G. (1995). *Direct simulation of spatially evolving compressible turbulent boundary layers.* Paper presented at the AIAA 950583, 33rd Aerospace Sciences Meeting and Exhibit, Reno, NV.

Schiller, L., & Naumann, A. Z. (1933). A Drag Coefficient Correlation. *Z. Ver. Deutsch Ing., 77*, 318-320.

Snyder, L. J., & Stewart, W. E. (1966). Velocity and pressure profiles for newtonian creeping flow in regular packed beds of spheres. *A.I.Ch.E.J., 12*(1), 167.

Sorensen, J. P., & Stewart, W. E. (1974). Computation of forced-convection in slow flow through ducts and packed-beds .2. velocity profile in a simple cubic array of spheres. *Chemical Engineering Science, 29*(3), 819-825.

Subramaniam, S. (2001). Statistical modeling of sprays using the droplet distribution function. *Physics of Fluids, 13*(3), 624-642.

Syamlal, M., Rogers, W., & O'Brien, T. J. (1993). *MFIX Documentation: Theory Guide*. Morgantown: National Energy Technology Laboratory.

van der Hoef, M. A., Beetstra, R., & Kuipers, J. A. M. (2005). Lattice-Boltzmann simulations of low-Reynolds-number flow past mono- and bidisperse arrays of spheres: results for the permeability and drag force. *Journal of Fluid Mechanics, 528*, 233-254.

Verzicco, R., Mohd-Yusof, J., Orlandi, P., & Haworth, D. (2000). Large eddy simulation in complex geometric configurations using boundary body forces. *AIAA Journal, 38*(3), 427-433.

Wylie, J. J., & Koch, D. L. (2000). Particle clustering due to hydrodynamic interactions. *Physics of Fluids, 12*(5), 964-970.

Xu, Y. (2008). *Modeling and direct numerical simulation of particle laden turbulent flows.* Iowa State University, Ames.

Yusof, J. M. (1996). Interaction of massive particles with turbulence. Cornell University, Ithaca.

Zick, A. A., & Homsy, G. M. (1982). Stokes flow through periodic arrays of spheres. J. Fluid Mech., 115, 13--26.